Journal of Nuclear Materials 401 (2010) 38–45

Contents lists available at ScienceDirect

Journal of Nuclear Materials

journal homepage: www.elsevier.com/locate/jnucmat

Structural stability and oxidation resistance of amorphous Zr–Al alloys

I.L. Soroka [a,*], J. Vegelius [b], P.T. Korelis [b], A. Fallberg [a], S.M. Butorin [b], B. Hjörvarsson [b]

[a] Department of Materials Chemistry, Uppsala University, Box 538, SE-751 21 Uppsala, Sweden
[b] Department of Physics and Materials Science, Uppsala University, Box 530, SE-751 21 Uppsala, Sweden

ARTICLE INFO

Article history:
Received 16 December 2009
Accepted 18 March 2010

ABSTRACT

We investigated the structural stability and oxidation resistance of Zr–Al films upon annealing in air. The concentration of Zr was varied from 0 to 100 at.%, with a step of 10 at.%. The films were fabricated using ultra-high vacuum based magnetron sputtering. The as-deposited films with Zr content from 17.3 at.% to 70.7 at.% were found to be X-ray amorphous at room temperature. When exposed to air a thin oxide layer, typically less than 6 nm, is formed. The thickness of the oxide layers increases when the samples are annealed in air and most of these are found to be fully oxidized at 700 °C with the formation of crystalline and amorphous oxides on the top of crystalline and amorphous metal films, respectively. The amorphous oxide layers are found to be dense, with well defined thicknesses. An experimental non-equilibrium phase diagram is provided, covering the whole concentration range of the Zr–Al system.

1. Introduction

One of the requirements that the in-core and cladding materials for nuclear reactors should fulfil is corrosion resistance and their ability to form and maintain protective surface layers [1]. As described in the literature [2] corrosion damage, namely, hydrogen and oxygen penetration into the material occurs predominantly at grain boundaries and dislocations [3,4]. One possible approach to reduce the corrosion rate is to use a grain-free material. The basic idea to eliminate all grain boundaries by using an amorphous material is illustrated in Fig. 1. Good corrosion resistance of amorphous materials can be attributed to their structural and chemical homogeneity as well as to the formation of a stable passive layer [5,6]. Often it is one of the alloy elements that is responsible for the formation of the surface layer, providing corrosion resistance [7,8].

Alloys based on the binary Zr–Al system have a low neutron absorption cross section [9] and form amorphous structures in a wide concentration range [10]. Furthermore, a protective amorphous oxide layer is formed on these alloys, which makes this material of potential interest for the use as a construction material for nuclear reactors. The importance of Zr-based amorphous materials is not restricted to these applications. Zr–Al alloys can also be used in the fabrication of multi-layered structures, where high-quality layering is observed [11]. The employment of the smooth amorphous layers causes an improved performance of the devices based on such structures [12].

Here, we address the structural stability and the oxidation behaviour of Zr–Al alloy films in a wide concentration range, upon annealing to 700 °C in air.

2. Experimental details

2.1. Samples preparation

Thin Zr–Al alloy films were produced by magnetron sputtering. The atomic concentration of Zr in the alloy films was varied in the range between 0 and 100 at.% with a step of 10%. All films were grown in an ultra-high vacuum chamber by co-sputtering on thermally oxidized Si (0 0 1)/SiO_2 substrates. The base pressure in the chamber was less than 3×10^{-10} Torr. Sputtering was carried out in an Ar atmosphere (purity: 99.999%) at 2.5 mTorr pressure and at room temperature from Zr (99.9%) and Al (99.999%) targets. The deposition rate was controlled by magnetron power inputs and adjusted to the flux ratio of the constituents. The total film thickness was selected in the range of 150 nm, which provides enough material for establishing the thermal stability of the films. The films of elemental Zr and Al were used as references.

The alloy samples are labelled as follows: Zr_XAl_Y, where X and Y correspond to the nominal atomic concentration of Zr and Al, respectively. This is obtained by the ratio of the atomic flux of the elements while growing the alloy films. The films labelled Zr_{100} and Al_{100} correspond to the pure elemental films.

All films were annealed in air: The first annealing was performed at 200 °C for 1 h and after cooling down in the furnace, the structure and morphology of the films was investigated. The procedure was repeated, with increasing temperature in steps of 100 °C, up to 700 °C, which was the final annealing temperature.

* Corresponding author. Tel.: +46 18252173.
E-mail address: Inna.Soroka66@gmail.com (I.L. Soroka).

0022-3115/$ - see front matter © 2010 Elsevier B.V. All rights reserved.
doi:10.1016/j.jnucmat.2010.03.016

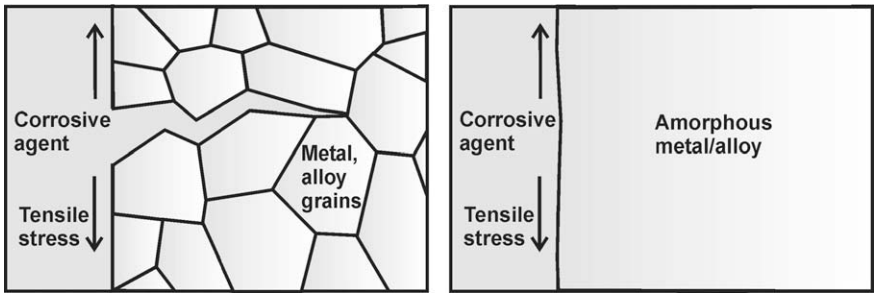

Fig. 1. Schematic illustration of stress corrosion cracking [2]. A corrosive agent diffuses through the opened crack and corrodes grain boundaries under stress (left image), while the corrosion rate is expected to be different in grain-free materials (right image).

2.2. Rutherford backscattering spectrometry

Rutherford backscattering spectrometry (RBS) was used to verify the composition of the films. All the measurements were performed at the Tandem accelerator laboratory in Uppsala. The incident single charged He^+ ions with primary beam energy of 2.00 MeV were detected at a scattering angle of 160°. The SIMNRA software [13] was used for the compositional analysis using the elemental films as a reference.

2.3. X-ray diffraction

The structural properties of the films were determined by X-ray reflectivity (XRR) and X-ray diffraction (XRD) measurements using a Siemens D5000 diffractometer in Bragg–Brentano geometry, with Cu Kα radiation at a wavelength $\lambda = 1.54$ Å.

2.4. X-ray spectroscopy

The electronic structures of the as-deposited films were studied by X-ray Absorption (XAS) and Emission (XES) Spectroscopy. The measurements were carried out at beam line 511-3 at MAX-lab in Lund, Sweden [14], which employs a plane-grating monochromator providing available energies between 90 and 1500 eV. XAS spectra were measured in the Total Electron Yield (TEY) mode using drain current on the samples. XAS in this mode is hence a surface-sensitive technique suitable for measuring thin oxide layers. XES was measured using a high-resolution grazing-incidence grating spectrometer [15]. The resolution of the monochromator during the experiment was set to 50 meV at 70 eV. The spectrometer resolution was 150 meV at 70 eV.

X-ray Photoelectron Spectroscopy (XPS) was used to determine the composition of the oxide layer that forms on the surface of as-deposited elemental Zr and Al films. It is a surface-sensitive technique which provides information on both the elemental composition and the chemical state for the near-surface region of solids. The elemental detection limit is typically 0.1 at.% so it is also sensitive to elements, which concentrations in the film is low [16]. The instrument used for sample excitation is an ESCA PHI Quantum 2000 with monochromatic Al Kα X-ray source at 1486.6 eV and 200 μm beam spot size. The depth profile of chemical shifts and film composition is obtained by measuring repeatedly after etching away a few top layers from the film using argon ion sputtering. A spectrum was recorded each time after etching for 30 s, with a sputtering energy of 0.5 keV, until the peak from oxygen O 1*s* disappeared. The sputtering time was then converted to a sample depth scale by combining XPS and XRR data.

2.5. Ellipsometry

On the heat-treated samples, ellipsometry measurements were conducted to complement the structural investigation. Ellipsometry gives information about the thickness and refractive index of the oxide layers by detecting the change in the state of polarization of light upon reflection. An Automatic Ellipsometer AutoEL^R-IL equipped with a laser with a single operating wavelength of 632.8 nm.

3. Results and discussion

3.1. Structure at room temperature

3.1.1. Amorphous vs. crystalline phases

The resulting composition of as-deposited films extracted from RBS measurements and the films structure obtained from X-ray study are summarized in Table 1. Note, the uncertainty in the alloy composition obtained from RBS measurements does not exceed 0.5 at.%.

As seen in the table, the alloy film compositions obtained from RBS measurements are close to the nominal values, confirming the reproducibility of the growth procedures. In particular, the difference in composition is found to be less than 3 at.% in all films.

XRD scans were carried out on all samples in the region $2\theta = 20$–$125°$. The diffraction patterns for as-deposited Al and Zr films as well as for $Zr_{60}Al_{40}$ are presented in Fig. 2. All diffraction curves contain the peaks from (0 0 1) plane of the Si (0 0 1) substrate, the first order at about 34° which is actually a forbidden reflection and the second order at 69.13°. The pure Zr film is found to be polycrystalline, since several diffraction peaks, corresponding to different atomic planes, are present in the XRD pattern [17]. The pattern for the pure Al film consists of the reflections from (1 1 1) planes pointing out to a textured structure. For the $Zr_{60}Al_{40}$ sample, only peaks from the substrate can be seen. The diffraction curve for the $Zr_{60}Al_{40}$ film that shown in Fig. 2 is characteristic for all samples with nominal Zr concentration in the range between 20 at.% and 70 at.%. Although the X-ray diffraction patterns support the absence of crystalline order, it is possible that some local order (e.g. nanocrystallites) is present in the films [18]. Nanocrystalline phases can be detected using TEM analysis which, however, is beyond the scope of present communication. Consequently the term

Table 1
The composition and structure of as-deposited alloy films.

Sample	Zr, at.%	Al, at.%	Hf, at.%	Structure
$Zr_{10}Al_{90}$	8.6	91.3	0.05	Crystalline
$Zr_{20}Al_{80}$	17.3	82.6	0.1	Amorphous
$Zr_{30}Al_{70}$	27.0	72.8	0.2	Amorphous
$Zr_{40}Al_{60}$	38.0	61.8	0.2	Amorphous
$Zr_{50}Al_{50}$	49.5	50.2	0.3	Amorphous
$Zr_{60}Al_{40}$	59.3	40.4	0.3	Amorphous
$Zr_{70}Al_{30}$	70.7	28.9	0.4	Amorphous
$Zr_{80}Al_{20}$	81.5	18.0	0.5	Crystalline
$Zr_{90}Al_{10}$	90.8	8.7	0.5	Crystalline

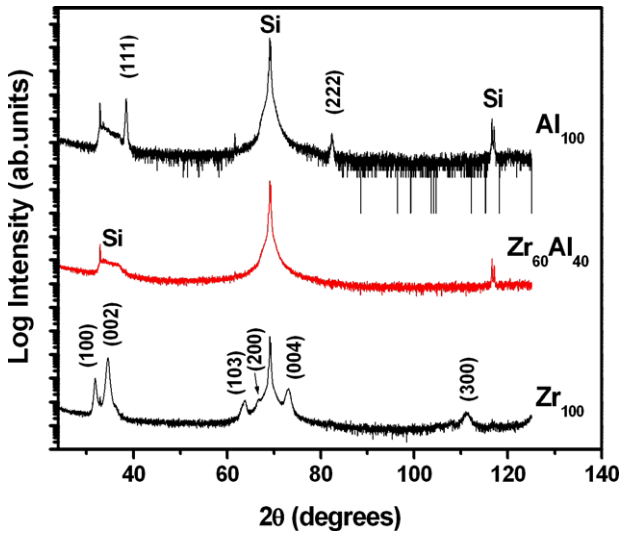

Fig. 2. X-ray diffraction pattern for as-deposited Al, Zr and $Zr_{60}Al_{40}$ films. The labels in the graph refer to the crystal planes orientations in the films. Note, that only diffraction peaks from the substrate are present in XRD pattern for $Zr_{60}Al_{40}$ film.

"amorphous" refers here to the absence of crystalline phases as determined by X-ray diffraction (X-ray amorphous).

The changes in the electronic structure of Al with transition from a crystalline to an amorphous state were probed by Soft X-ray emission measurements. The emission spectra at the Al *L*2,3 edge (3*s*, 3*d* → 2*p* transitions) are shown in Fig. 3 for some representative samples.

As seen in the figure, spectrum features such as the peak positions and broadening are quite different for pure aluminium film (Al_{100}) as compared to the alloys. In particular, the sharp peak at 72.5 eV, representing the contribution of the Al 3*s* and 3*d* states appears at the top of the valence band for the crystalline Al film, while this peak becomes significantly broader and shifts towards lower energy in the amorphous alloys. This difference can be ascribed to hybridization effect in the alloys. Similar behaviour has previously been observed in other aluminium based alloys [19]. Moreover, as seen in the figure, there is a rather small difference in the relative intensities of two peaks located at about 67 and 72 eV (see Fig. 3) between the spectra of $Zr_{60}Al_{40}$ and $Zr_{40}Al_{60}$ alloys as compared to that between $Zr_{40}Al_{60}$ and $Zr_{20}Al_{80}$ films.

In case of alloying effect alone, gradual changes are expected in the spectra due to changes in hybridization with Zr states, while non-gradual changes are observed here. To explain this behaviour one needs to consider the structure of $Zr_{20}Al_{80}$ alloys with respect to that of $Zr_{40}Al_{60}$ and $Zr_{60}Al_{40}$. According to previous studies, Zr–Al films with less than 17% Zr were found to be either in crystalline state [20] or on the border between the amorphous and crystalline states [21,22]. In the current study, a $Zr_{20}Al_{80}$ alloy film is found to be X-ray amorphous, and as it is shown in Section 3.4, it crystallizes at a temperature above 200 °C apart from $Zr_{40}Al_{60}$ and $Zr_{60}Al_{40}$ films which remain amorphous even at 700 °C. Therefore, one can expect that the stability of the amorphous phase in $Zr_{40}Al_{60}$ and $Zr_{60}Al_{40}$ alloys is higher as compared to that in $Zr_{20}Al_{80}$. Hence, the non-gradual changes in the alloy spectra can be ascribed to the structural changes in the alloys as well as to hybridization effects.

3.1.2. Oxidation

All the films form an oxide layer upon exposure to air. The thickness of the oxide layers was determined using X-ray reflectivity measurements and representative results are displayed in Fig. 4. Note, that the results for the $Zr_{40}Al_{60}$ and $Zr_{60}Al_{40}$ samples are characteristic for all films with amorphous structure. Finite size oscillations which correspond to the total film thickness are clearly visible for all samples. Low-frequency oscillations (with a period of about 1°), which arise from the thin oxide layer on the top of the films, are also present. Simulation of the shape of the reflectivity curves allows us to determine both the total thickness of the films as well as the thickness of the oxide layer. Note, the finite size oscillations from the amorphous $Zr_{40}Al_{60}$ and $Zr_{60}Al_{40}$ films are more pronounced, as compared to the elemental films, and also appear over a bigger range in 2θ.

All the spectra were simulated using the X'Pert Reflectivity software. The film thicknesses were found to be 140 ± 10 nm and the thickness of the top oxide layer is 4 ± 2 nm. There is large uncertainty in the oxide layer thickness that originates from the oxide layer being much thinner relatively to the total film thickness. Thus, scattering from the oxide layer produces finite thickness oscillations with a much lower frequency that are superimposed on the

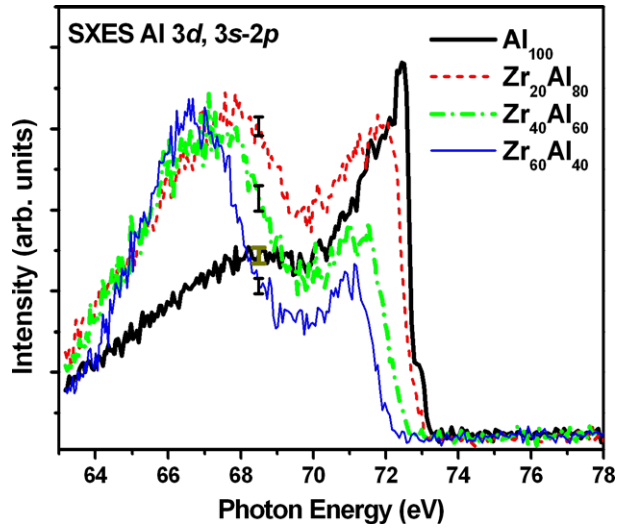

Fig. 3. Al *L*2,3 X-ray emission spectra. The spectra show transitions from Al 3*s*, 3*d* valence band states to the core 2*p* level. The spectra are normalized to their maximum and no background was subtracted. The excitation energy is 82 eV. The standard deviation of the intensity is shown at 68.5 eV.

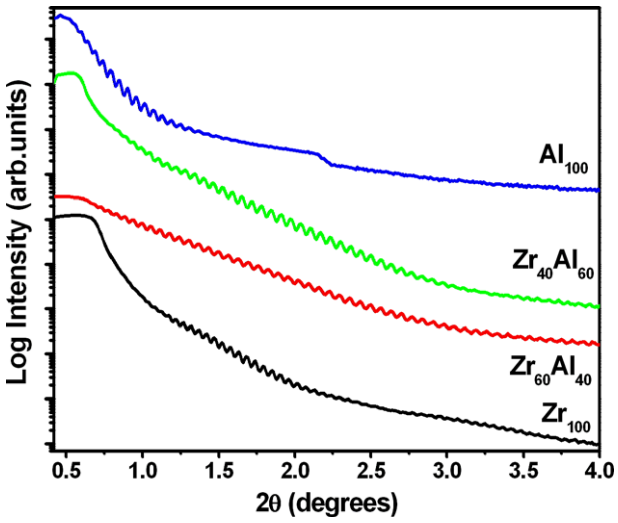

Fig. 4. Reflectivity spectra for as-deposited Zr–Al alloy films. The finite size oscillations correspond to the total film thicknesses.

total reflectivity curve. These two contributions are convoluted in the reflectivity curve and are parameters in the fitting process.

The correlated film roughness was determined to be $\sigma = 1.0$–1.5 nm from these simulations. This holds for all films with the exception of the Al_{100} and $Zr_{10}Al_{90}$ samples, which have larger layer thickness variation.

The photoelectron spectrum on Zr 3*d* states from the Zr_{100} sample (Fig. 5a) consists of two peaks which correspond to Zr $3d_{3/2}$ (the lower binding energy) and Zr $3d_{5/2}$ (the higher binding energy). Both peaks shift towards lower energy with increasing film depth indicating gradual decrease of the Zr oxidation state. Four different chemical environments for Zr have been observed at different film depth. Near the surface, the film consists of stoichiometric ZrO_2 [23]. Underneath that, two suboxidic contributions are found. They correspond to oxide material having gradients of Zr-enrichment and O-deficiency. This suggests that the defect structure in this part consists of both oxygen vacancies and Zr interstitials [24,25]. The last spectra collected at the deepest point in the sample, corresponds to elemental Zr.

The O 1*s* spectra from the surface of the Zr_{100} film (Fig. 5b) include one peak at a binding energy of 529.9 eV. This corresponds to zirconium dioxide [23]. Another peak for the oxygen atoms below the sample surface lies at 531.4 eV. In previous studies [25], this was attributed to ZrO_X. However, the same binding energy is characteristic for $Zr(OH)_4$ as well and the possibility that this phase is present in the oxide layers cannot be disproven [23]. The intensity of the oxygen peak is gradually reduced the deeper the etching goes and it finally disappears, which suggests that the underlying film consists of pure Zr. The observed behaviour is typical for the oxidation of metals at low temperatures, where the diffusion of Zr or O through the oxide film is negligibly small [26].

In the photoelectron spectrum on the Al 2*p* state for the Al_{100} film, see Fig. 6a, two near-surface related peaks are observed. The corresponding binding energies are 72.8 eV and 75.4 eV which is characteristic for pure Al metal [23] and Al^{3+} [27], respectively. In the oxygen 1*s* spectrum for the same sample, Fig. 6b, a peak at 532.2 eV is observed which corresponds to O^{2-} [27]. Thus, both aluminium and Al_2O_3 are present in the near-surface region. Etching deeper, the observed chemical shifts towards higher energies for aluminium as well as for oxygen core levels, indicate the presence of both non-stoichiometric oxide and aluminium hydroxide [23].

The binding energy depends on the type of atom the electron came from as well as the environment it came from. Increasing covalent character of the metal oxygen bonds in Al_2O_3 as compared to ZrO_2 causes an increase in the chemical shifts of oxygen. Thus, the binding energy of oxygen in ZrO_2 is lower than in Al_2O_3.

The carbon content in the Zr_{100} and Al_{100} films is found to be negligible both on the surfaces and throughout the films, using XPS.

The composition variation of the top oxide layers as a function of the alloy concentration was studied by Soft X-ray Absorption Spectroscopy (XAS). Data was recorded at the oxygen K edge (transitions from 1*s* to unoccupied *p*-states of oxygen) and representative results are shown in Fig. 7. The absorption spectra of the Zr_{100} and Al_{100} samples look like those of ZrO_2 and Al_2O_3, respectively [28–30].

According to McComb et al. [28,29] the O–K absorption spectrum is sensitive to the crystal structure of the zirconium oxide. Note, the spectrum that corresponds to the Zr_{100} film mostly resembles the tetragonal phase of ZrO_2. Phase transition between crystalline and amorphous states is hence expected to be seen in the XAS measurements. Unlike the case of Al 2*p* emission spectra described earlier, alterations between different compositions resulted in gradual changes in the spectra throughout the whole range of Zr content. These changes are a result of hybridization of O *p*-states with Zr and Al states. The observed spectral behaviour indicates the absence of phase transitions in the oxide layers, i.e. the oxide layers on all the films are either amorphous or crystalline.

In summary, Zr–Al alloy films with thickness of about 150 nm are found to be X-ray amorphous in the Zr concentration range from 17.3 to 70.7 at.% at room temperature. Thin oxide layers form on the top of all films when exposed to air after deposition. The composition of these oxide layers varies from sample to sample, following the changes in the film composition. The depth profile of the oxygen concentration for pure Zr and Al films shows that it is gradually decreasing with depth until it becomes negligible inside the films.

3.2. Phase transition and oxidation behaviour at elevated temperatures

After the room temperature measurements, the samples were annealed in air. All films were first annealed at 200 °C for 1 h. This was repeated in steps of 100 °C up to 700 °C. The XRR, XRD and ellipsometry measurements performed between the annealing steps indicate that during heat-treatment the films undergo both

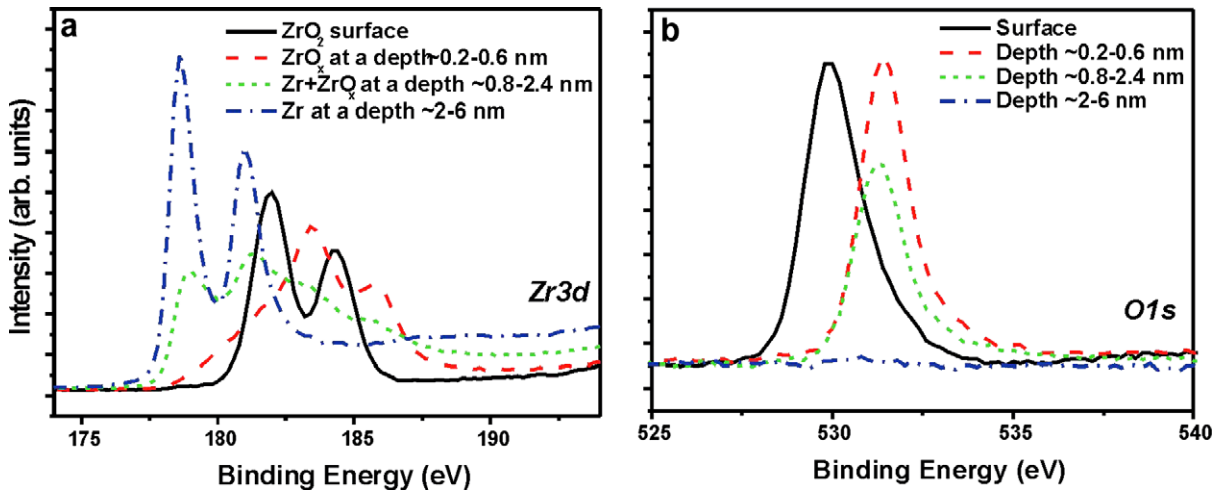

Fig. 5. XPS spectra of Zr 3*d* (a) and O 1*s* (b) recorded from Zr_{100} sample. The lines indicated with different colour and type correspond to the spectra taken from different depth of the film. (For interpretation of the references to colour in this figure legend, the reader is referred to the web version of this article.)

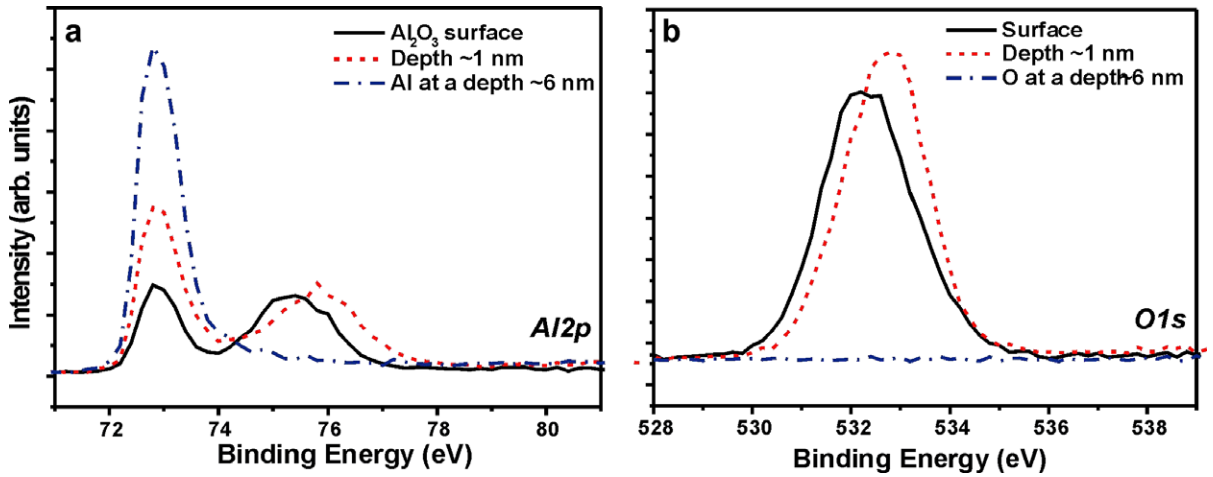

Fig. 6. XPS spectra of Al 2*p* (a) and O 1*s* (b) recorded from Al_{100} sample. The lines indicated with different colour and type correspond to the spectra taken from different depth of the film. (For interpretation of the references to colour in this figure legend, the reader is referred to the web version of this article.)

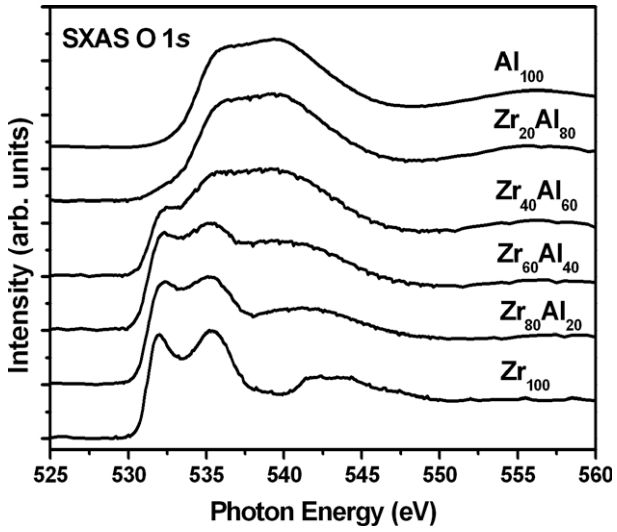

Fig. 7. X-ray absorption spectra at the O–K edge. The spectra are normalized to their maximum respectively and no background was subtracted.

a phase transition and changes in their chemical composition through oxidation. The results allow the classification of the samples in three groups, according to similarities in their structure and their oxidation behaviour. The grouping is done according to the Zr-to-Al ratio which is found to be the most influential factor on the film properties.

The *first group* includes the films from Zr_{100} to $Zr_{80}Al_{20}$. Characteristic XRD spectra from the $Zr_{90}Al_{10}$ sample in this group can be seen in Fig. 8(1). The XRD pattern from the as-deposited films consists of diffraction peaks originating from the metal film and from the substrate. It is evident that the positions of the diffraction peaks from the film correlate with those identified in the pattern for the as-deposited Zr_{100} film, see Fig. 2. As expected, the peak positions from the metal films shift gradually towards higher angles with increasing Al concentration (not shown here). The average inter-atomic distance decreases with increasing Al concentration, as Al atoms are smaller than Zr.

As seen in Fig. 8(1) the intensity of the XRD peaks from the metal film starts to decrease after heating at 300 °C, while peaks from Zr dioxide appear [31,32]. With still higher temperatures, the peaks from the metallic film disappear, while the intensity of the diffraction peaks from the oxide layer increases significantly. Consequently, the as-deposited films in this group have a polycrystalline structure which gradually transforms to a polycrystalline oxide after heat-treatment in air.

The *second group* contains the films with intermediate alloy composition, from $Zr_{70}Al_{30}$ to $Zr_{30}Al_{70}$. Initially, these films are X-ray amorphous and no change in the diffraction pattern is observed upon heat-treatment. Typical XRD spectra from $Zr_{40}Al_{60}$ are presented in Fig. 8(2). The only contribution to the diffraction is coming from the silicon substrate at all temperatures investigated here.

Reflectivity measurements before and after heat-treatment (not shown here) indicate that the total film thickness increases. Oscillations of a lower frequency are apparent, consistent with increasing thickness of the oxide layer. These changes can also be observed by the change in colour, arising from interference effects in the oxide layer. An exception in the above picture is the $Zr_{30}Al_{70}$ sample. Up to 300 °C it maintains an amorphous structure while after raising the temperature to 400 °C some crystalline phases of Al and Zr are identified through the XRD analysis. However, the sample appears to favour an amorphous configuration at higher temperatures and at 700 °C it is transformed to an amorphous oxide phase.

The *third group* consists of the Al-rich films, $Zr_{10}Al_{90}$, $Zr_{20}Al_{80}$ and Al_{100}. Typical spectra from Al_{100} are shown in Fig. 8(3). A common attribute of those films is that the total film thickness remains unchanged up to 400 °C. Up to this temperature the surface of the samples has a characteristic metallic shine. At and above 500 °C it begins to tarnish indicating that the thickness of the oxide layer increases. However, the existence of crystalline oxide and metallic phases is detected from the XRD analysis, which supports incomplete oxidation.

The aluminium film, Al_{100}, is completely oxidized upon annealing at 700 °C. Furthermore, the thickness of the oxide layer was determined to be 52 ± 10 nm by ellipsometry. Thus, its thickness is significantly reduced. The annealing temperature of 700 °C is above the melting temperature of Al (660 °C [33]). Thus evaporation is highly likely to have taken place, or a chemical reaction with the underlying substrate might have occurred. Diffraction peaks arising from aluminium oxide, Al_XO_Y [34] appear after the film was heated at 700 °C. Moreover, a peak at $2\theta \approx 28°$ is identified as a reflection from aluminium oxide silicate, $Al_2(SiO_4)O$. All films are grown on Si/SiO_2 substrates, so the formation of silicates at elevated temperatures is probable [35].

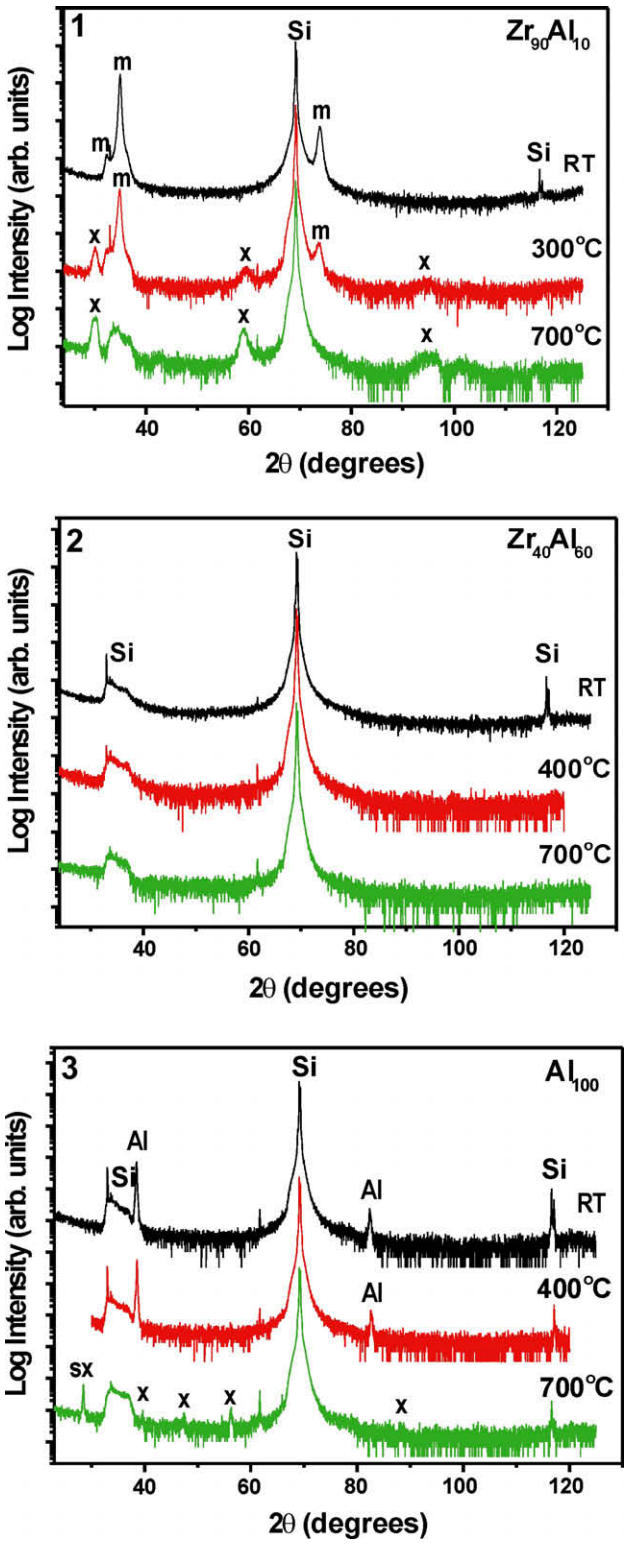

Fig. 8. The typical X-ray diffraction patterns for the Al–Zr films classified into three groups: (1) Polycrystalline Zr-rich films. The reflections from the metal/alloy and from Zr dioxide are labelled with "m" and "x", respectively; (2) Amorphous film; (3) Polycrystalline Al-rich films. The oxides and silicates are labelled with "x" and "sx", respectively. The numbers on the graphs correspond to the annealing temperatures. Observe that peaks from Si substrate are present in all XRD patterns.

3.3. Thermal stability in air

A natural oxide layer forms on top of all as-deposited samples when exposed to air. It appears to be stable up to a certain temperature which differs between groups and so does its rate of expansion at elevated temperatures. There exist similar trends in the oxidation behaviour of the samples belonging to each of the above-mentioned groups. This is further established by plotting the thickness of the oxide layer as a function of temperature for each group, see Fig. 9. The oxide layers thicknesses were obtained analytically by combining results from both XRR and

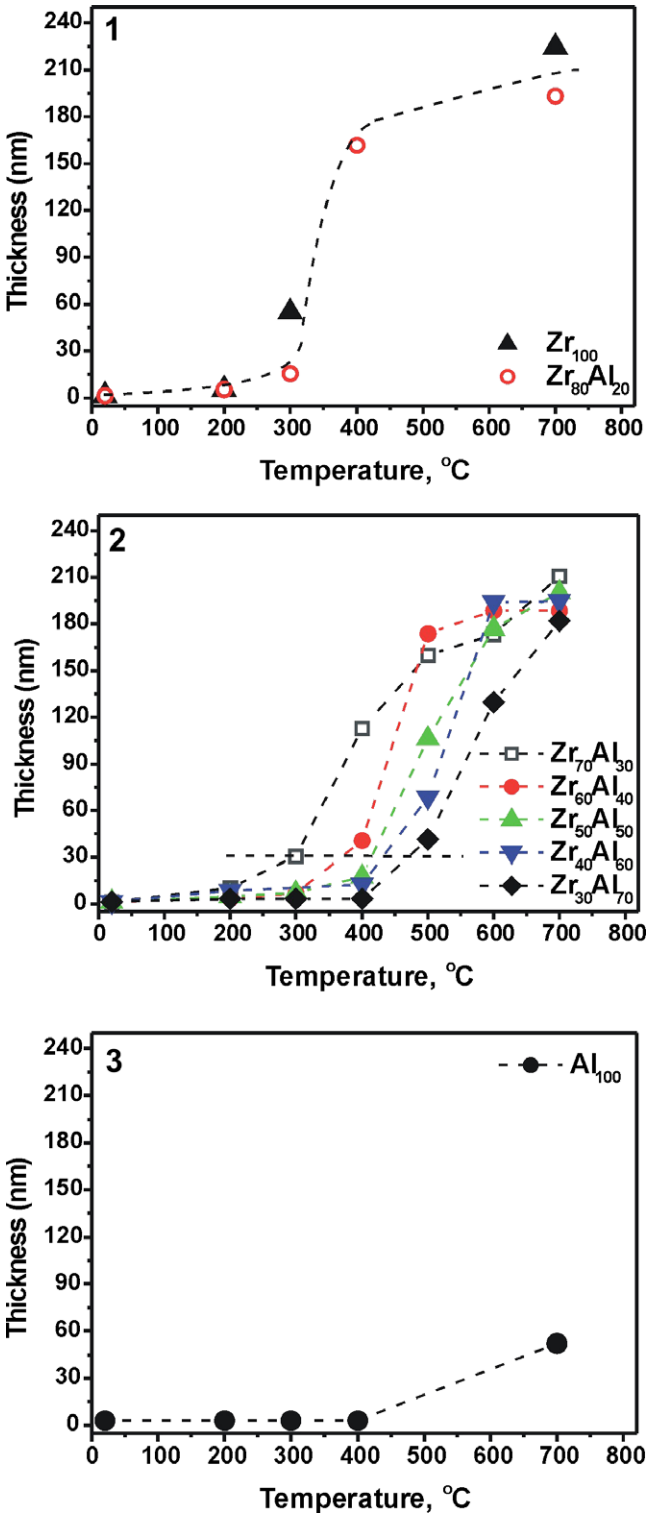

Fig. 9. The thickness of the oxide layers vs. the heating temperature in Zr–Al films classified into three groups. The size of the points corresponds to the uncertainty in the film thickness determination.

ellipsometry measurements. Here, the ellipsometry measurements are used mostly to determine the thickness of those oxide layers whose roughness is rather large and therefore, their thickness is not possible to determine by XRR measurements. The sizes of the points in Fig. 9 correspond to the uncertainty in the thickness determination.

The Zr-rich crystalline films of *the first group*, Fig. 9(1), start to oxidize further when the temperature exceeds 300 °C, and at still higher temperatures the films are fully oxidized.

The oxidation resistance for the amorphous films in *the second group*, Fig. 9(2), reveals a strong dependency on composition. The dashed line in Fig. 9 indicates the temperature required for the formation of a 30 nm thick oxide layer. This temperature has a reciprocal dependence on zirconium concentration it is increased with decreasing zirconium concentration. This highlights the Al as the key element responsible for the thermal stability and the passivation properties of the protective oxide layers formed on the Zr–Al alloy films. The increase of oxide layer thickness, ΔTh, with increasing temperature, ΔT, can be determined from the slope in the figure. The average value for $\Delta Th/\Delta T$ is higher for the zirconium-rich crystalline films (see Fig. 9(1)) as compared to the amorphous films, Fig. 9(2), yielding values of 1.5 nm/degree and 0.8 nm/degree, respectively. The amorphous films with high aluminium content were found to be the most resilient to oxidation as the temperature increases.

The aluminium-rich films of *the third group* undergo no structural changes for temperatures up to 400 °C, when the oxide layer starts growing slowly until it reaches an average thickness of 60 nm at 700 °C, Fig. 9(3). Since the oxidation curves for $Zr_{20}Al_{80}$ and $Zr_{10}Al_{90}$ are completely overlapping with that for the Al_{100} sample, only one curve for the Al_{100} film is presented on the graph. It appears that in spite of the thermal cycling, oxidation in these films does not progress as fast as in Zr–Al samples of the first and second group in the observed temperature window. Moreover, the films' surfaces lost their metallic shine, a finding consistent with increasing surface roughness.

3.4. Non-equilibrium low-temperature phase diagram for Zr–Al films

All findings are summed up in a phase diagram for the Zr–Al system in Fig. 10. The presence of metal/oxide and amorphous/crystalline states are displayed as a function of temperature and alloy concentration. The separation lines on the diagram correspond to composition–temperature coordinates where a sudden change in the structure or oxide layer thickness is observed.

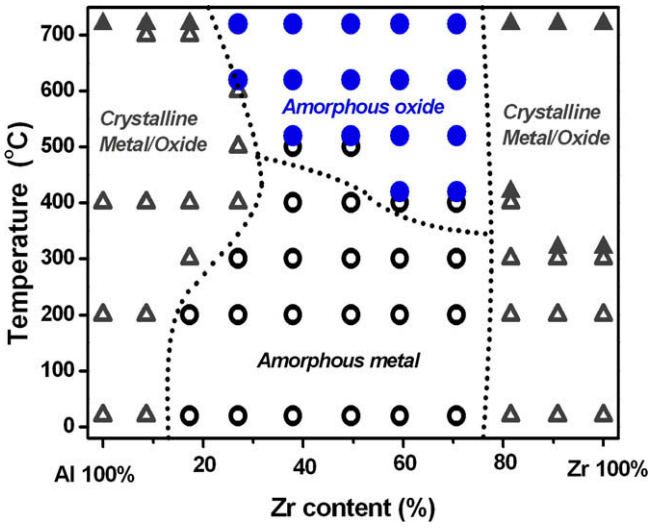

Fig. 10. The phase diagram of Zr–Al alloyed films. The open and filled circles correspond to amorphous metal and amorphous oxide films, respectively. The open and filled triangulates correspond to metal and oxide crystalline state, respectively. Note, that all metallic films contain thin oxide layers on the top.

As seen in the figure, four regions may be distinguished in the phase diagram: Zr-rich, Al-rich and intermediate one, divided into low- and high-temperature regions. In the Zr-rich and Al-rich regions, the films have polycrystalline structure after deposition, and their crystallinity is maintained while the metal films gradually become oxidized with increasing temperatures. The amorphous films with nominal zirconium concentration ranging from 17.3 at.% to 70.7 at.% remain stable up to 400 °C and at higher temperatures the sample oxidation produces a smooth oxide layer on top of the film. In the concentration range between 38 at.% and 70.7 at.% Zr both the film and the oxide layer stays amorphous regardless the temperature and the degree of oxidation.

4. Conclusions

The structural stability and oxidation resistance of Zr–Al films fabricated by magnetron sputtering technique in ultra-high vacuum conditions and with Zr concentration in the range from 0 to 100 at.% with the step of 10%, have been studied at different temperatures.

The as-deposited films with Zr content from 17.3 at.% to 70.7 at.% are found to be X-ray amorphous. Thin oxide layers, less than 6 nm in thickness, are formed on the top of the films at ambient conditions. The depth profile measurements made on Zr and Al films reveal that the oxygen concentration gradually decreases with the depth and becomes negligible inside the films. The amount of carbon in the films was determined to be below the detection limit of the XPS equipment.

The transition from amorphous to crystalline state with increasing annealing temperature was observed in Al-rich (from 17.3 up to 27 at.% Zr) alloy films. For Zr concentrations in the range between 38 at.% and 70.7 at.% both the film and the oxide structures remain amorphous regardless the temperature and the degree of oxidation. Zr-rich films with Zr content greater than or equal to 81.5 at.% undergo a transition from crystalline metallic to crystalline oxide states.

The chemical stability of the amorphous films increases with increasing Al content. This proves that Al is responsible for the formation of passivating layers on the samples. Moreover, the increase of the oxide thickness with temperature for amorphous films occurs less steeply than for the crystalline films of higher Zr concentration. This may indicate higher oxidation resistance of amorphous as compared to that of crystalline materials. Al-rich crystalline films demonstrate good thermodynamic stability, however, the quality of their surface degrades quickly at temperatures above 400 °C.

All the findings are summarized in the form of a non-equilibrium phase diagram that covers the whole concentration range of the Zr–Al system.

Acknowledgments

This work has been supported by the Carl Tryggers Foundation (CTS), the Swedish Research Council (VR) and the Knut and Alice Wallenberg Foundation (KAW). I.L.S. would like to thank Dr. Bručas for help with the ellipsometry measurements and for the fruitful discussions. P.T.K. would like to thank Dr. Bojan Zajec from the Jožef Stefan Institute for his help in rebuilding the RBS setup as well as Jonas Åström and Gösta Widman for their support at the Tandem Laboratory at Uppsala University.

References

[1] C.E. Lucas, J. Nucl. Mater. 216 (1994) 322–325.
[2] M. Itakura, H. Kaburaki, C. Arakawa, Phys. Rev. E 71 (2005). 055102-1–4.
[3] V. Fidleris, J. Nucl. Mater. 159 (1988) 22–42.
[4] M. Griffiths, R.A. Holt, A. Rogerson, J. Nucl. Mater. 225 (1995) 245–258.
[5] M. Naka, K. Hashimoto, T. Masumoto, J. Non-Cryst. Solids 30 (1978) 29–36; M. Naka, K. Hashimoto, T. Masumoto, J. Non-Cryst. Solids 31 (1979) 355–365.
[6] T.M. Devine, J. Electrochem. Soc. 124 (1977) 38–44.
[7] V. Schroeder, R.O. Ritchie, Acta Mater. 54 (2006) 1785–1794.
[8] M.K. Tam, S.J. Pang, C.H. Shek, J. Phys. Chem. Solids 67 (2006) 762–766.
[9] U. Rösler, Siemens Rev. 33 (3) (1966) 211–215.
[10] E. Ma, F. Brunner, M. Atzmon, J. Phase. Equilib. 14 (1993) 137–141.
[11] H. Raanaei, H. Nguyen, G. Andersson, H. Lidbaum, P. Korelis, K. Leifer, B. Hjörvarsson, J. Appl. Phys. 106 (2009). 023918-1–7.
[12] D. Carvalho, S. Cardoso, R. Vilar, Scripta Mater. 37 (1997) 523–527.
[13] M. Mayer, SIMNRA User's Guide. Tech. Rep. IPP 9/113, Max-Planck-Institut für Plasmaphysik, Garching, 1997.
[14] R. Denecke, P. Vaterlein, M. Bassler, N. Wassdahl, S. Butorin, A. Nilsson, J.-E. Rubensson, J. Nordgren, N. Martensson, R. Nyholm, J. Electron Spectrosc. Relat. Phenom. 101 (1999) 971–977.
[15] J. Nordgren, R. Nyholm, Nucl. Instrum. Methods Phys. Rs. A 246 (1986) 242–245.
[16] E.L. Principe, R.W. Odom, A.L. Johnson, G.D. Ackermann, Z. Hussain, H. Padmore, Mater. Res. Soc. Symp. Proc. 524 (1998) 221–226.
[17] Swanson, Fuyat, Natl. Bur. Stand. (U.S.), Circ. 539 II, vol. 11, 1953.
[18] A. Gajović, D. Gracin, I. Djerdj, Appl. Surf. Sci. 254 (2008) 2748–2754.
[19] D.L. Ederer, R. Schaefer, K.-L. Tsang, C.H. Zhang, T.A. Callcott, E.T. Arakawa, Phys. Rev. B 15 (1988) 8594–8597.
[20] J.-K. Ho, K.-L. Lin, J. Appl. Phys. 75 (1994) 2434–2440.
[21] H. Yoshioka, H. Habazaki, A. Kawashima, K. Asami, K. Hashimoto, Electochem. Acta 36 (1991) 1227–1233.
[22] J.J. Yang, Y. Yang, K. Wu, J. Appl. Phys. 98 (2005). 074508-1–6.
[23] T.L. Barr, J. Phys. Chem. 82 (1978) 1801–1810.
[24] A. Lyapin, L.P.H. Jeurgens, P.C.J. Graat, E.J. Mittemeijer, J. Appl. Phys. 96 (2004) 7126–7135.
[25] L.P.H. Jeurgens, A. Lyapin, E.J. Mittemeijer, Surf. Interface Anal. 38 (2006) 727–730.
[26] A. Lyapin, L.P.H. Jeurgens, P.C.J. Graat, E.J. Mittemeijer, Surf. Interface Anal. 36 (2004) 989–992.
[27] C. Hinnen, D. Imbert, J.M. Siffre, P. Marcus, Appl. Surf. Sci. 78 (1994) 219–231.
[28] D.W. McComb, Phys. Rev. B 54 (1996) 7094–7102.
[29] D.W. McComb, S. Ostanin, D. Vlachos, A.J. Craven, M.W. Finnis, A.T. Paxton, A. Alavi, Mater. Res. Soc. Symp. 699 (2002) 161–166.
[30] T. Sasaki, K. Matsunaga, H. Ohta, H. Hosono, T. Yamamoto, Y. Ikuhara, Sci. Technol. Adv. Mater. 4 (2003) 575–584.
[31] L.M. Lityagina, S.S. Kabalkina, T.A. Pashkina, A.I. Khozyainov, Sov. Phys. Solid State 20 (1978) 2009–2010.
[32] H. Boysen, F. Frey, T. Vogt, Acta Crystallogr., Sec. B: Struct. Sci. 47 (1991) 881–886.
[33] M. Hansen, K. Aderko, Constitution of Binary Alloys, McGraw-Hill, New York, 1958.
[34] E. Husson, Y. Repelin, Eur. J. Solid State Inorg. Chem. 33 (1996) 1223–1231.
[35] T.L. Alford, P.K. Shetty, N.D. Theodore, N. Tile, D. Adams, J.W. Mayer, Thin Solid Films 516 (2008) 3940–3947.